CHEMISTRY OF MATERIALS

pubs.acs.org/cm

Article

Exploring the Morphotropic Phase Boundary in Epitaxial $PbHf_{1-x}Ti_xO_3$ Thin Films

Megha Acharya, Handong Ling, Djamila Lou, Maya Ramesh, Brendan Hanrahan, Gabriel Velarde, Mark Asta, Kristin Persson, and Lane W. Martin*

Cite This: *Chem. Mater.* 2022, 34, 9613−9623

Read Online

ACCESS | Metrics & More | Article Recommendations | Supporting Information

ABSTRACT: Epitaxial $PbHf_{1-x}Ti_xO_3/SrTiO_3(001)$ thin-film heterostructures are studied for a potential morphotropic phase boundary (MPB) akin to that in the $PbZr_{1-x}Ti_xO_3$ system. End members, $PbHfO_3$ and $PbTiO_3$, were found to possess orthorhombic (*Pbam*) and tetragonal (*P4mm*) crystal structures and antiferroelectric and ferroelectric (~87 $\mu C/cm^2$) behavior, respectively. $PbHf_{0.75}Ti_{0.25}O_3$ and $PbHf_{0.25}Ti_{0.75}O_3$ solid solutions were both found to be ferroelectric with rhombohedral (*R3c*, ~22 $\mu C/cm^2$) and tetragonal (*P4mm*, ~46 $\mu C/cm^2$) structures, respectively. For intermediate $PbHf_{1-x}Ti_xO_3$ compositions (e.g., x = 0.4, 0.45, 0.5, and 0.55), a structural transition was observed from rhombohedral (hafnium-rich) to tetragonal (titanium-rich) phases. These intermediate compositions also exhibited mixed-phase structures including *R3c*, monoclinic (*Cm*), and *P4mm* symmetries and, in all cases, were ferroelectric with remanent (5−22 $\mu C/cm^2$) and saturation (18.5−36 $\mu C/cm^2$) polarization and coercive field (24−34.5 kV/cm) values increasing with x. While the dielectric constant was the largest for $PbHf_{0.6}Ti_{0.4}O_3$, the MPB is thought to be near x = 0.5 after separation of the intrinsic and extrinsic contributions to the dielectric response. Furthermore, piezoelectric displacement−voltage hysteresis loops were obtained for all chemistries revealing displacement values as good as $PbZr_{0.52}Ti_{0.48}O_3$ films in the same geometry. Thereby, the $PbHf_{1-x}Ti_xO_3$ system is a viable alternative to the $PbZr_{1-x}Ti_xO_3$ system offering comparable performance.

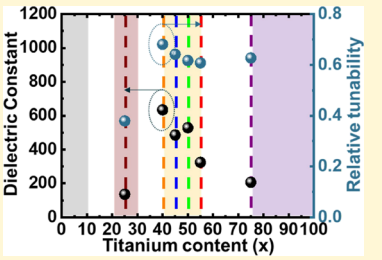

INTRODUCTION

Some of the best performing piezoelectrics are ferroelectric materials that exhibit large magnitudes of spontaneous polarization where the motion of domain walls can enhance the electromechanical response. Among the various families of piezoelectric ferroelectrics, $PbZr_{1-x}Ti_xO_3$ has been used extensively as both sintered ceramics and thin films for a multitude of applications including sensors, ultrasonic transducers, voltage-tunable capacitors, resonators, surface acoustic wave devices (e.g., filters, phase shifters, phase delay lines), electro-optic modulators, microelectromechanical system (MEMS)-based devices, and so on.[1−5] The $PbZr_{1-x}Ti_xO_3$ system is of particular interest because it exhibits a nearly temperature-independent phase boundary (at x = 0.48) called a morphotropic phase boundary (MPB) about which the material possesses outstanding dielectric and electromechanical properties.[6−8] The mechanism for enhancement of the piezoelectric response at the MPB is thought to be related to the ease of rotation of the polar axis from rhombohedral to tetragonal phases facilitated by the presence of an intermediate monoclinic phase whose polar axis is expected to be contained along a direction in between that of the rhombohedral and tetragonal phases.[9−12]

Thin films of $PbZr_{1-x}Ti_xO_3$ can, however, suffer from deleterious effects including polarization fatigue (degradation with read-write cycles) and retention (degradation with time), imprint, and low breakdown strength and switching speed.[13−17] Additionally, the integration of epitaxially grown $PbZr_{1-x}Ti_xO_3$ thin films on non-oxide semiconductor substrates for MEMS or CMOS processes can be challenging.[1,3,5,18,19] Epitaxial growth of $PbZr_{1-x}Ti_xO_3$ films on silicon requires high temperatures and oxidizing environments that increase the risk of forming interfacial phases.[19,20] In turn, identifying silicon-compatible functional oxides with dielectric, piezoelectric, and ferroelectric properties comparable to that of $PbZr_{1-x}Ti_xO_3$ has become increasingly important as these materials are being considered for a range of next-generation devices. While zirconium and hafnium are chemically similar,[21−23] zirconium exhibits higher reactivity with silicon[24] as compared to hafnium. The energetics of the reactions involved were further confirmed using the *Interfaces Reaction* application[25,26] in the *Materials Project*[27] platform by comparing the reaction-energy values for the interfacial reactions of $PbHfO_3$ and $PbZrO_3$ with SiO_2 as a function of mixing ratios (Figure S1a,b). Such effects have also been seen in recent experiments where, for example, a study on $Hf_{1-x}Zr_xO_2$ films grown on silicon used the zirconium for in

Received: July 28, 2022
Revised: October 16, 2022
Published: October 27, 2022

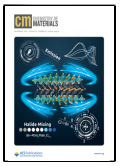

situ scavenging of the interfacial SiO_2.[28] At the same time, the discovery of ferroelectricity in HfO_2-based materials[29] has driven a resurgence in efforts to integrate HfO_2-based ferroelectrics directly on silicon.[30−32] Experimental trials with atomic layer deposition on silicon using hafnia-based precursors have been as successful as that with the zirconia-based precursors.[33]

In the current work, we build from these lessons and explore the MPB in the $PbHf_{1-x}Ti_xO_3$ ($0 < x < 1$) system which is analogous to $PbZr_{1-x}Ti_xO_3$.[34,35] Previous studies on $PbHf_{1-x}Ti_xO_3$ bulk ceramics and polycrystalline films report the presence of an MPB near $PbHf_{0.5}Ti_{0.5}O_3$.[33,36−45] Additionally, a few reports have suggested an improvement in fatigue and imprint behavior in certain compositions of polycrystalline $PbHf_{1-x}Ti_xO_3$ thin films as compared to that in $PbZr_{1-x}Ti_xO_3$.[36,39] This, combined with the higher compatibility of the growth process, further motivates the need to more extensively study $PbHf_{1-x}Ti_xO_3$ as epitaxial thin films and probe the composition-driven evolution in the crystal structure and dielectric, piezoelectric, and ferroelectric properties. In this spirit, here, highly crystalline, fully relaxed, and epitaxial $PbHf_{1-x}Ti_xO_3$ (x = 0, 0.25, 0.4, 0.45, 0.5, 0.55, 0.75, and 1) thin films are synthesized on $SrRuO_3/SrTiO_3(001)$ substrates. Using X-ray diffraction, the crystal structure and lattice parameters of the films are examined. Similar to the $PbZr_{1-x}Ti_xO_3$ system, a structural phase transition is observed as the ratio of Ti^{4+} (ionic radius of 0.61 Å) to Hf^{4+} (ionic radius of 0.76 Å) is varied wherein the $PbHf_{1-x}Ti_xO_3$ system goes from an orthorhombic (*Pbam*) phase for $PbHfO_3$[46] to a rhombohedral (*R*3*c*) phase for $PbHf_{0.75}Ti_{0.25}O_3$ to a mixed-phase regime (i.e., a mixture of rhombohedral *R*3*c*, monoclinic *Cm*, and tetragonal *P*4*mm* phases) in the range x = 0.4−0.55, before finally transitioning to a purely tetragonal (*P*4*mm*) phase for $PbHf_{0.25}Ti_{0.75}O_3$ and $PbTiO_3$. Subsequent study of ferroelectric polarization-electric field hysteresis loops reveals a transition from antiferroelectric behavior for the x = 0 heterostructures to ferroelectric behavior in the composition range x = 0.25−1. The remanent and saturation polarization and the coercive-field values increase with increasing titanium content owing to the larger magnitude of polar displacement (again consistent with the $PbZr_{1-x}Ti_xO_3$ system). Furthermore, composition-dependent dielectric constant (ε_r) measurements indicate an enhancement in the dielectric response in the composition range x = 0.4−0.55 that is attributed to the coexistence of the rhombohedral, monoclinic, and tetragonal phases and the ease of polarization rotation therein. Field-dependent studies of ε_r are used to estimate the intrinsic and extrinsic contributions to response, and the maximum intrinsic response is found for $PbHf_{0.5}Ti_{0.5}O_3$ heterostructures (the likely location of the MPB) while the maximum extrinsic response was found for $PbHf_{0.6}Ti_{0.4}O_3$ heterostructures (pointing to the presence of a comparatively mobile-domain configuration). The piezoelectric response of heterostructures of all compositions was measured using piezoresponse force microscopy (PFM) and laser Doppler vibrometry and compared to that of films of $PbZr_{0.52}Ti_{0.48}O_3$ of the same thickness and geometry. The piezoresponse of the $PbHf_{1-x}Ti_xO_3$ films, especially near the MPB, was found to be comparable to that of $PbZr_{0.52}Ti_{0.48}O_3$, further reinforcing the similarity between the two material systems as well as the potential for the use of this system in applications calling for low-loss, high-performance piezoelectric thin films.[47,48]

EXPERIMENTAL SECTION

Growth of Thin-Film Heterostructures. 50−200 nm-thick $PbHf_{1-x}Ti_xO_3$ (x = 0, 0.25, 0.4, 0.45, 0.5, 0.55, 0.75, and 1) thin-film heterostructures were synthesized on (001)-oriented $SrTiO_3$ substrates using pulsed-laser deposition. 35−45 nm-thick $SrRuO_3$ layers were used as the conducting oxide for both the top and bottom electrodes. Pulsed-laser deposition was performed by ablating ceramic targets using a KrF excimer laser (248 nm, LPX 300, Coherent), in an on-axis geometry with the target-to-substrate distance of 55 mm. Multiple growth conditions and target chemistries were explored for synthesizing the parent compositions (i.e., $PbHfO_3$ and $PbTiO_3$). The best results were obtained for $PbHfO_3$ ($PbTiO_3$) heterostructures grown on $SrTiO_3(001)$ substrates at a laser fluence of 1.93 J/cm^2, a laser repetition rate of 10 Hz (5 Hz), a heater temperature of 600 °C (650 °C), and a dynamic oxygen pressure of 10 mTorr (100 mTorr) and using ceramic targets with composition $PbHfO_3$ ($Pb_{1.1}TiO_3$). The $PbHf_{1-x}Ti_xO_3$ solid solutions (x = 0.25, 0.4, 0.45, 0.5, 0.55, and 0.75) were synthesized using two different routes. The first case involved synthesis using alternate ablation from the two parent targets (i.e., $PbHfO_3$ and $PbTiO_3$) with sub-unit-cell-level mixing using a programmable target rotator (Neocera, LLC) synced with the excimer laser. In this approach, by alternating pulses from the different targets in the right proportions, any composition can be obtained. In the other case, individual targets with compositions $PbHf_{1-x}Ti_xO_3$ (x = 0.4, 0.45, 0.5, and 0.55) were used for synthesizing the heterostructures. For thin-film heterostructures with compositions $PbHf_{0.75}Ti_{0.25}O_3$ and $PbHf_{0.25}Ti_{0.75}O_3$, the best results were obtained with the first route (i.e., with alternate ablation from two parent targets), while for compositions $PbHf_{1-x}Ti_xO_3$ (x = 0.4, 0.45, 0.5, 0.55) the best results were obtained with the second route (i.e., ablation from a single target). For all growths, the heterostructures were cooled from the growth temperature to room temperature at 10 °C/min. in a static oxygen pressure of ∼760 Torr.

Structural Characterization Using X-ray Diffraction. X-ray diffraction studies were performed to determine the crystal structure of the synthesized $PbHf_{1-x}Ti_xO_3$ (x = 0, 0.25, 0.4, 0.45, 0.5, 0.55, 0.75, and 1) thin-film heterostructures with a high-resolution X-ray diffractometer (Panalytical, X'Pert^3 MRD) using 1/2° and 1/16° slits for the incident optics and a 0.275 mm slit for the diffracted-beam optics for the PIXcel3D-Medipix3 detector. The structural properties of the thin films in the out-of-plane direction (perpendicular to the plane of the substrate) were probed using θ−2θ line scans. The crystalline quality of the films in the plane of the substrate was assessed using X-ray rocking curves about the 002_{pc}-diffraction condition of all heterostructures. Furthermore, (a)symmetric azimuthal scans were carried out about the $PbHf_{1-x}Ti_xO_3$ $1\bar{1}8_R$- and 006_R- (for $PbHf_{0.75}Ti_{0.25}O_3$ heterostructures), $20\bar{2}_M$- (for $PbHf_{0.5}Ti_{0.5}O_3$ heterostructures), and 112_T- and 101_T- (for $PbHf_{0.25}Ti_{0.75}O_3$ heterostructures) diffraction conditions while varying the azimuthal angle (φ) at a fixed 2θ and sample-stage tilt (χ) value. Additionally, in order to determine the crystal structure and the lattice parameters of the heterostructures with composition $PbHf_{1-x}Ti_xO_3$ (x = 0, 0.25, 0.4, 0.45, 0.5, 0.55, 0.75, and 1), X-ray diffraction reciprocal space mapping (RSM) studies were performed about the 362_O- and 084_O-diffraction conditions ($PbHfO_3$), 103_{pc}- and 202_{pc}-diffraction conditions [$PbHf_{1-x}Ti_xO_3$ (x = 0.25, 0.4, 0.45, 0.5, 0.55, 0.75, and 1)] of the films and $SrTiO_3$ 103-diffraction condition of the $SrTiO_3$ substrate, as appropriate.

Electrical and Dielectric Characterization. All electrical measurements were conducted in a dark and noise-isolated enclosure with the drive electrical bias applied through the top electrode. The electrical properties for heterostructures of all compositions [$PbHf_{1-x}Ti_xO_3$ (x = 0, 0.25, 0.4, 0.45, 0.5, 0.55, 0.75, and 1)] were studied for 50−200 nm-thick films grown on $SrTiO_3(001)$ substrates. While all the synthesized heterostructures could be characterized successfully, the temperature-dependent dielectric characterization was found to be challenging for the $PbHf_{1-x}Ti_xO_3$ films less than 200 nm thick owing to a high dielectric loss factor (>0.1). We point out that this is generally common in thin films and was variable across the

https://doi.org/10.1021/acs.chemmater.2c02295
Chem. Mater. 2022, 34, 9613−9623

compositions studied. To provide directly comparable results, in turn, we focused on results obtained for 200 nm-thick $PbHf_{1-x}Ti_xO_3$ heterostructures. Furthermore, 45- and 35-nm-thick films of a conducting oxide, $SrRuO_3$, were used as the top and bottom electrodes, respectively. A relatively thicker film was used for the top electrode as compared to that for the bottom electrode to counteract for any potential degradation in the quality of the top electrode, having been synthesized at a slightly lower temperature (650 °C) as compared to the bottom electrode (700 °C). The thicker top electrode also allows it to be more robust to repeated contacting for measurements using micropositioner-based probes."

The measurements were performed with circular-capacitor (diameter 25 μm) structures patterned on the top electrode using photolithography, followed by wet chemical etching of $SrRuO_3$ via a 0.1 M $NaIO_4$ solution. The polarization values were measured as a function of electric field (−650 to 650 kV/cm) at room temperature using a Precision Multiferroic Tester (Radiant Technologies, Inc.). Prior to any dielectric measurements, all the capacitors were switched 50−60 times and poled with a bias of a magnitude −1 V with a dwell time of 1 s. Dielectric and loss tangent measurements were performed as a function of frequency (1−100 kHz), temperature (25−550 °C), DC electric field (−250 to 250 kV/cm), and up to a maximum AC field strength value of 50 kV/cm using an E4990A Impedance Analyzer (Keysight Technologies). For the frequency-dependent DC bias measurements, an AC signal with an excitation amplitude of 10 mV (which translates to a field of 0.5 kV/cm) was applied with the frequency being varied between 1 and 100 kHz for a fixed applied background DC bias. The applied background DC bias was varied from 0 to −250 kV/cm with a step size of 5 kV/cm. For the Rayleigh measurements (AC excitation-dependent studies), an AC signal was applied, and its excitation amplitude was varied from 0 to 50 kV/cm at a fixed frequency of 10 kHz while maintaining zero background bias.

Electromechanical Characterization with PFM. The localized piezoelectric displacement hysteresis loops were measured as a function of an applied voltage via switching spectroscopy-based PFM using an MFP-3D (Asylum Research). The applied voltage was in the form of a sine wave (AC excitation signal) which is carried by a square wave (DC bias) which steps up or down in magnitude as a function of time (in the form of a triangular-square pulse). Between each voltage step, the DC bias offset is set to zero while the AC excitation is still active, to determine the bias-induced change in displacement. This displacement was measured as a function of applied DC bias continuously while cycling the pulse 5−10 times (each cycle has a duration of 5 s).

Electromechanical Characterization with Laser Doppler Vibrometry. For the macroscopic electromechanical surface displacement studies, the heterostructures were electrically stimulated with an AC-excitation field (−350 to 350 kV/cm) at a frequency of 10 kHz using a ferroelectric tester (Precision Multiferroic Tester, Radiant Technologies, Inc.) while a 2 μm-sized HeNe laser (λ = 633 nm) spot was focused on the surface of the 50 μm-diameter top electrode. Upon applying electrical field, the capacitor structure will be displaced vertically along the path of the laser owing to the macroscopic electromechanical response of the heterostructures. The magnitude of the response was monitored using a laser vibrometer (PolyTech GmbH) with a sensitivity of 5 nm/V. Based on the electrical feedback received from the vibrometer, the surface piezoelectric displacement values were determined as a function of electric field using the ferroelectric tester.

First-Principles Density Functional Perturbation Theory (DFPT) Calculations. Piezoelectric tensors and force constants are calculated for $PbHf_{1-x}Ti_xO_3$ compositions of 2 × 2 × 1 supercells of the perovskite structure comprising 20 atoms. The calculations were performed for certain selected $PbHf_{1-x}Ti_xO_3$ compositions with x = 0, 0.25, 0.5, 0.75, and 1, where the titanium content was increased from x = 0 to 1 for two different parent compounds, that is, the rhombohedral and the tetragonal crystal structure. The composition $PbHf_{0.5}Ti_{0.5}O_3$ was found to exhibit two distinct cation orderings for the supercell in consideration. The piezoelectric and dielectric tensors of these systems are calculated using DFPT,[49−52] utilizing the Vienna ab initio simulation package[53,54] within the PBE generalized gradient approximation (GGA+U).[55] An energy cut-off for the plane waves is set at 1000 eV with a k-point density of approximately 2000 per reciprocal atom (pra) for the DFPT calculations.[56] The resulting piezoelectric and dielectric values reported are the maximum modulus of the total tensors.

RESULTS AND DISCUSSION

50−200 nm-thick $PbHf_{1-x}Ti_xO_3$ (x = 0, 0.25, 0.4, 0.45, 0.5, 0.55, 0.75, and 1) thin-film heterostructures were grown on 45 nm $SrRuO_3/SrTiO_3$(001) substrates using pulsed-laser deposition as noted in the Experimental Section. Following growth, X-ray diffraction was used to study the structure and epitaxy of the films as noted in the Experimental Section. Before discussing the results, it is useful to explore what is known about the crystal structures of this system. The end member $PbHfO_3$ is known to be antiferroelectric and to exhibit an orthorhombic crystal structure (*Pbam*; Figure 1a).[46] Three

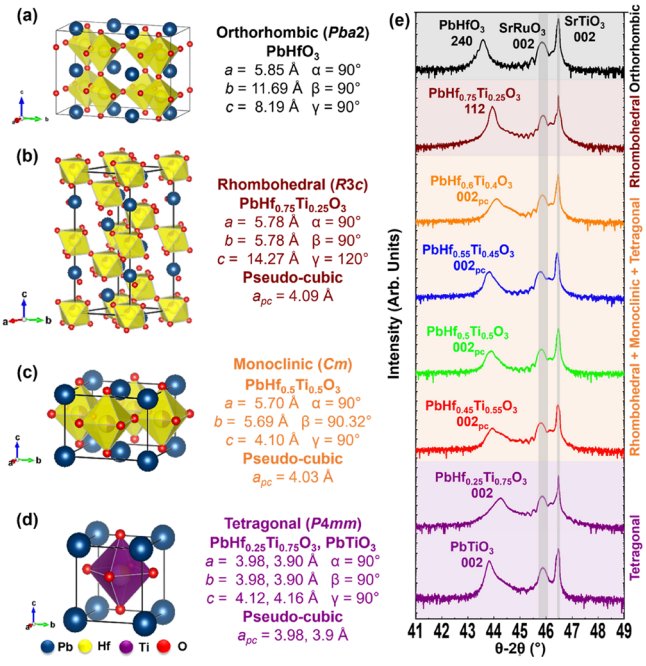

Figure 1. Crystal structure and lattice parameters for (a) the orthorhombic (*Pba*2) antiferroelectric phase of $PbHfO_3$, (b) the rhombohedral (*R*3*c*) ferroelectric phase of $PbHf_{0.75}Ti_{0.25}O_3$, (c) the monoclinic (*Cm*) ferroelectric phase of $PbHf_{0.5}Ti_{0.5}O_3$, and (d) the tetragonal (*P*4*mm*) ferroelectric phase of $PbHf_{0.25}Ti_{0.75}O_3$ and $PbTiO_3$. (e) X-ray-diffraction measurements (θ−2θ line scan) for 200-nm-thick, (240_O)-oriented $PbHfO_3$, $1\bar{1}2_R$-oriented $PbHf_{0.75}Ti_{0.25}O_3$, and 002_{pc}-oriented $PbHf_{1-x}Ti_xO_3$ (with x = 0.4, 0.45, 0.5, 0.55, 0.75, and 1) heterostructures grown on 40 nm $SrRuO_3/SrTiO_3$(001) substrates.

types of crystal structures have been reported for bulk-ceramic versions of $PbHf_{1-x}Ti_xO_3$: (1) rhombohedral (*R*3*c*; Figure 1b) for $x \leq 0.5$, (2) monoclinic (*Cm*; Figure 1c) for $PbHf_{0.5}Ti_{0.5}O_3$, and (3) tetragonal (*P*4*mm*; Figure 1d) for $x \geq 0.6$.[42,43,57] Looking now at the films produced herein, in all cases, the films were found to be single crystalline and phase-pure (Figure 1e). End-member $PbHfO_3$ heterostructures were fully (240_O)-oriented (where the subscript 'O' refers to orthorhombic indices) and end-member $PbTiO_3$ heterostructures were fully (001)-oriented and exhibited a tetragonal crystal

https://doi.org/10.1021/acs.chemmater.2c02295
Chem. Mater. 2022, 34, 9613−9623

structure. Using θ–2θ line scans (Figure 1e) and RSM studies about the 084_O- and 362_O- (for $PbHfO_3$ heterostructures; Figure S2) and 103- and 202-diffraction conditions (for $PbTiO_3$ heterostructures; Figure S3), the crystal structure and lattice parameters were extracted (Table S1).

Exact attribution of the crystal structure for single-crystalline thin films is somewhat challenging because of the limited number of diffraction conditions accessible through laboratory-based diffractometers. From prior studies on bulk ceramics, the $PbHf_{0.75}Ti_{0.25}O_3$ and $PbHf_{0.25}Ti_{0.75}O_3$ heterostructures were expected to exhibit rhombohedral (*R*3*c*) and tetragonal (*P*4*mm*) structures, respectively. To evaluate if this was the case here, azimuthal scans about the *R*3*c* $1\bar{1}8_R$- (2θ = 54.57°, sample-stage tilt (χ) = 35.33, where the subscript 'R' stands for lattice indexing corresponding to rhombohedral structure) and *P*4*mm* 112- (2θ = 55.25°, sample-stage tilt (χ) = 36.22) diffraction conditions were completed. From this, the presence (absence) of rhombohedral (tetragonal) and tetragonal (rhombohedral) phases in the $PbHf_{0.25}Ti_{0.75}O_3$ and $PbHf_{0.75}Ti_{0.25}O_3$ heterostructures, respectively, was confirmed (Figure S4). In prior studies on $PbHf_{0.5}Ti_{0.5}O_3$ ceramics, the crystal structure was found to be predominantly monoclinic (*Cm*); however, being close to the phase boundary, it also contained a minor phase with rhombohedral (*R*3*c*) symmetry.[42,57] Using the same azimuthal-scan methodology, but now looking for the monoclinic *Cm* $20\bar{2}_M$-diffraction condition (2θ = 54.94°, sample-stage tilt (χ) = 35.86, where the subscript 'M' stands for lattice indexing corresponding to monoclinic structure) along with that for the rhombohedral and tetragonal phases (noted above), we explored the compositions near the 'potential' phase boundary (i.e., x = 0.4–0.55 heterostructures; Figure S5). As expected, the compositions demonstrated non-zero peak intensity for all three diffraction conditions indicating a complex mixture of phases with *R*3*c*, *Cm*, and *P*4*mm* symmetry. To further understand the nature of the structure for these mixed-phase compositions, the peak profile corresponding to the 003_{pc}-diffraction condition for these heterostructures was fit using Voigt functions to estimate the volume fraction of the three phases (i.e., *R*3*c*, *Cm*, and *P*4*mm*; Figure S6). The mixed-phase heterostructures (i.e., x = 0.4–0.55) exhibited different volume fractions of *R*3*c* (23.5–32.4%), *Cm* (27.5–61.3%), and *P*4*mm* (9.5–49%) phases. Akin to the end-member films, the lattice parameters corresponding to the rhombohedral ($PbHf_{0.75}Ti_{0.25}O_3$), mixed-phase (x = 0.4–0.55), and tetragonal ($PbHf_{0.25}Ti_{0.75}O_3$) heterostructures were determined (Figures S7 and S8) and summarized (Table S1). All heterostructures were found to be fully relaxed, consistent with the large lattice mismatch between the $PbHf_{1-x}Ti_xO_3$ films and the substrate. For the compositions with mixed-phase and tetragonal structures, the *c*/*a* ratio (tetragonality) was found to increase with increasing titanium content, which can be interpreted as an increasing volume fraction of the tetragonal phase.[44] Knowing the crystal structure and the lattice parameters, the epitaxial relationship of the synthesized heterostructures to the substrate was also determined using off-axis azimuthal scans as noted in the Experimental Section. While the rhombohedral ($PbHf_{0.75}Ti_{0.25}O_3$) end member was found to exhibit two rotational variants (I and II) with the corresponding epitaxy as $PbHf_{0.75}Ti_{0.25}O_3[100_R]||SrTiO_3[100]$ and $PbHf_{0.75}Ti_{0.25}O_3[100_R]||SrTiO_3[010]$ (Figure S9), the (predominantly) monoclinic mixed-phase heterostructures (i.e., x = 0.4–0.55) were found to be single-variant with the epitaxy as $PbHf_{1-x}Ti_xO_3$ (x = 0.4–0.55)$[110_M]||SrTiO_3[100]$ (Figure S10). The tetragonal ($PbHf_{0.25}Ti_{0.75}O_3$) end member, on the other hand, was found to be single-variant and to exhibit relatively simplistic epitaxy such that $PbHf_{0.25}Ti_{0.75}O_3[100]||SrTiO_3[100]$ (Figure S11).

The structure, as expected, varies dramatically with chemistry and, considering that the polarization depends strongly on structure, the ferroelectric properties should also vary. Capacitor structures were fabricated as noted in the Experimental Section and ferroelectric hysteresis loops were measured as a function of electric field (at a frequency of 10 kHz) for all heterostructures as noted in the Experimental Section (Figure 2). Starting with the $PbHfO_3$ heterostructures,

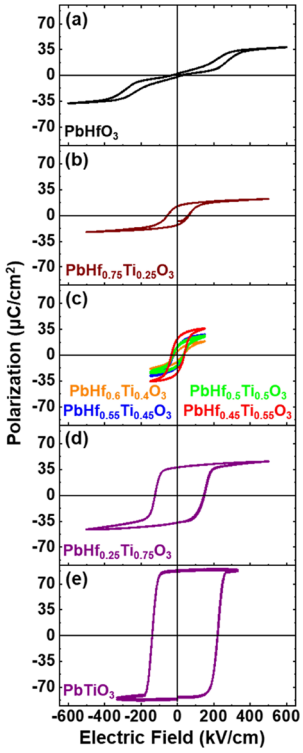

Figure 2. Polarization-electric field hysteresis loops at a frequency of 10 kHz for capacitors 25 μm in diameter for (a) the orthorhombic (*Pba*2) antiferroelectric phase of $PbHfO_3$, (b) the rhombohedral (*R*3*c*) ferroelectric phase of $PbHf_{0.75}Ti_{0.25}O_3$, (c) the mixed-phase ferroelectric $PbHf_{1-x}Ti_xO_3$ x = 0.4, 0.45, 0.5, and 0.55 compositions, and tetragonal (*P*4*mm*) ferroelectric phases of (d) $PbHf_{0.25}Ti_{0.75}O_3$ and (e) $PbTiO_3$.

which are known to be robustly antiferroelectric, a characteristic double-hysteresis loop was observed indicating an electric field-induced phase transition from a nonpolar (*Pbam*) to a polar, ferroelectric (*Pba*2) phase with a maximum polarization of ~53 $\mu C/cm^2$ at 1600 kV/cm (Figures 2a and S12). As even a relatively small amount of titanium is incorporated, as in the $PbHf_{0.75}Ti_{0.25}O_3$ heterostructures, ferroelectric behavior (with remanent and saturation polarization of ~12.5 and ~22 $\mu C/cm^2$, respectively, and a coercive field ~60 kV/cm) is observed, consistent with the crystal structure changing from orthorhombic to rhombohedral symmetry. Upon further increasing the titanium content (as in the x = 0.4–0.55 heterostructures), ferroelectric behavior is retained and the remanent (~5, ~11, ~12, and ~22 $\mu C/cm^2$, respectively) and saturation (~18.5, ~28, ~27, and ~36 $\mu C/cm^2$, respectively) polarization and the

https://doi.org/10.1021/acs.chemmater.2c02295
Chem. Mater. 2022, 34, 9613–9623

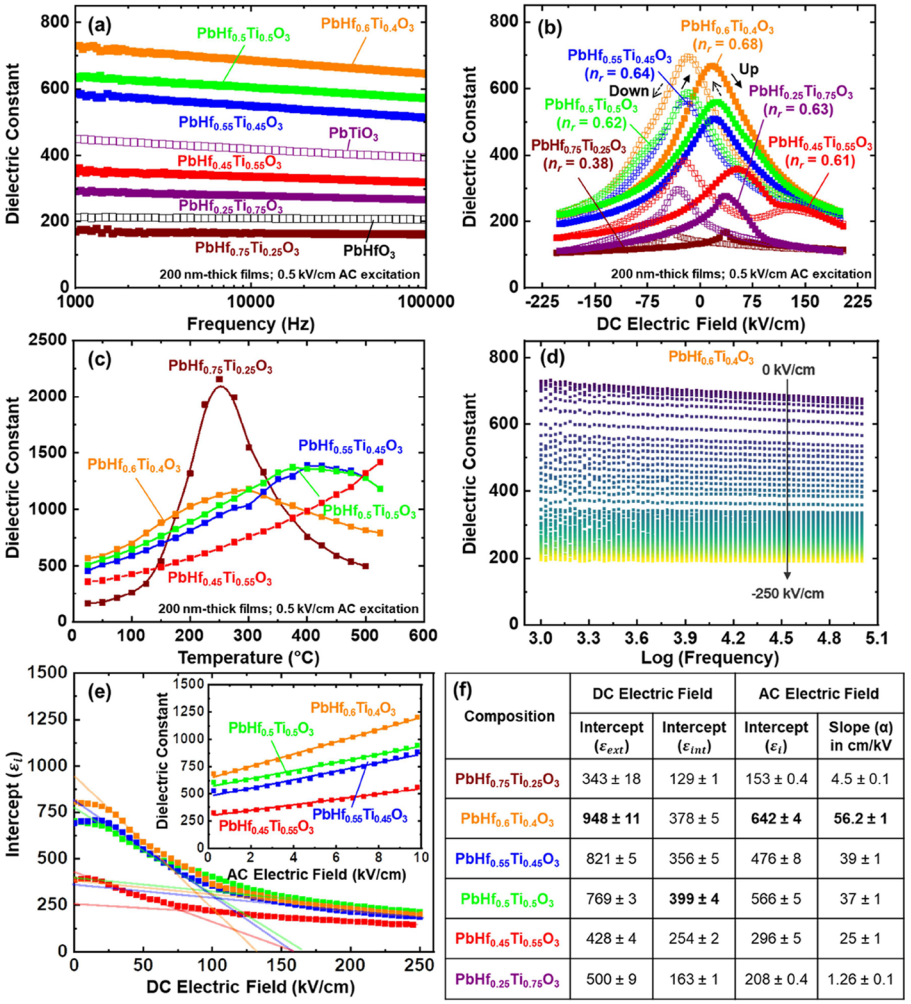

(f)

Composition	DC Electric Field		AC Electric Field	
	Intercept (ε_{ext})	Intercept (ε_{int})	Intercept (ε_i)	Slope (α) in cm/kV
$PbHf_{0.75}Ti_{0.25}O_3$	343 ± 18	129 ± 1	153 ± 0.4	4.5 ± 0.1
$PbHf_{0.6}Ti_{0.4}O_3$	**948 ± 11**	378 ± 5	**642 ± 4**	**56.2 ± 1**
$PbHf_{0.55}Ti_{0.45}O_3$	821 ± 5	356 ± 5	476 ± 8	39 ± 1
$PbHf_{0.5}Ti_{0.5}O_3$	769 ± 3	**399 ± 4**	566 ± 5	37 ± 1
$PbHf_{0.45}Ti_{0.55}O_3$	428 ± 4	254 ± 2	296 ± 5	25 ± 1
$PbHf_{0.25}Ti_{0.75}O_3$	500 ± 9	163 ± 1	208 ± 0.4	1.26 ± 0.1

Figure 3. Dielectric constant measurements for $PbHf_{1-x}Ti_xO_3$ heterostructures with x = 0, 0.25, 0.4, 0.45, 0.5, 0.55, 0.75, and 1 (a) as a function of frequency from 1 to 1000 kHz and (b) as a function of background DC field at frequency 10 kHz with two different voltage sweep directions (marked by solid and hollow squares for up and down, respectively). (c) Dielectric constant measurements of $PbHf_{1-x}Ti_xO_3$ heterostructures with x = 0, 0.25, 0.4, 0.45, 0.5, and 0.55 as a function of temperature (25−525 °C) at 10 kHz. (d) Dielectric constant as a function of frequency measured with increasing background DC field for a $PbHf_{0.6}Ti_{0.4}O_3$ heterostructure. (e) Plot of zero-field dielectric constant (ε_i) as a function of background DC field. The inset shows dielectric constant (ε_r) as a function of AC excitation for $PbHf_{1-x}Ti_xO_3$ heterostructures with x = 0.4−0.55. (f) Summary of the fitting parameters for the DC and AC-field dependent measurements.

coercive field (~24, ~27, ~30, and ~34.5 kV/cm, respectively) were all found to gradually increase with x. This is consistent with a systematic increase in the polar displacement (tetragonality) with increasing titanium content. Increasing the titanium content further, as in the $PbHf_{0.25}Ti_{0.75}O_3$ heterostructures, results in a tetragonal structure and further increases in the remanent (38 $\mu C/cm^2$) and saturation (46 $\mu C/cm^2$) polarization as well as the coercive field (130 kV/cm). Finally, for the $PbTiO_3$ heterostructures (with the highest tetragonality), the remanent and saturation polarization (87 $\mu C/cm^2$) and the coercive field (179 kV/cm) were found to be the highest across the $PbHf_{1-x}Ti_xO_3$ system. All told, an increase in polar displacement (polarization) with increasing titanium content was accompanied by an increase in the coercive field (because the magnitude of spontaneous polarization for a ferroelectric is directly proportional to the intrinsic coercive field).[58,59] On a mesoscopic scale, a higher energy associated with the nucleation and motion of 180° domains walls in tetragonal phases during switching can further increase the coercive field values.[60] Thereby, in parallel to a structural phase transition from the rhombohedral to tetragonal phase with increasing titanium content (x = 0.25 to 1), a simultaneous increase in remanent and saturation polarization and coercive field values was observed, likely to be due to the increasing volume fraction of tetragonal phase.

Having studied the structural and ferroelectric properties of single- and mixed-phase (anti)ferroelectric compositions for $PbHf_{1-x}Ti_xO_3$, we now focus on the primary realm of interest: the properties of the mixed-phase compositions (x = 0.4−0.55) in the vicinity of the expected MPB. We begin by measuring the frequency-dependent ε_r as noted in the Experimental Section as a function of composition (Figure 3a). All heterostructures exhibit minimal frequency dependence of response (across the frequencies studied), and the ε_r increases moving from both end-member compositions and is a maximum for the $PbHf_{0.6}Ti_{0.4}O_3$ heterostructures. The ε_r was also probed as a function of DC-background bias (Figure 3b) to explore dielectric tunability (n_r).[61,62] As expected, the highest tunability was observed in the vicinity of the MPB

https://doi.org/10.1021/acs.chemmater.2c02295
Chem. Mater. 2022, 34, 9613−9623

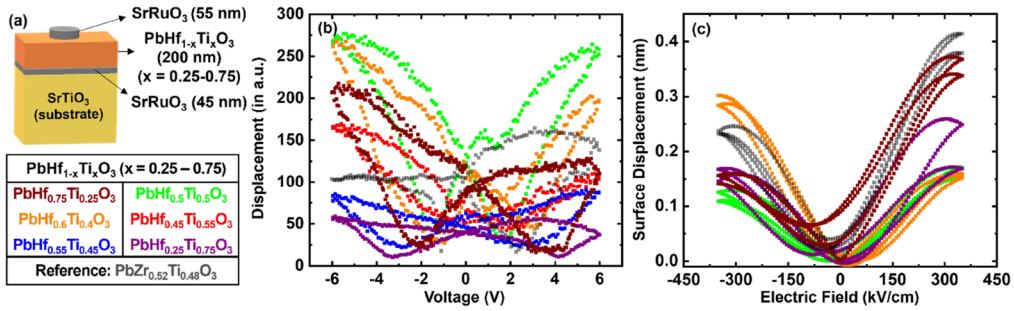

Figure 4. Electromechanical response measurements of $PbHf_{1-x}Ti_xO_3$ heterostructures with x = 0.25, 0.4, 0.45, 0.5, 0.55, and 0.75. (a) Schematic of the capacitor geometry and key of samples (colors are consistent throughout the figure). (b) Using switching spectroscopy in PFM at a frequency of 0.2 Hz, piezoelectric displacement−voltage butterfly loops were acquired. (c) Macroscopic surface displacement butterfly loops were acquired from 50 μm-diameter capacitors using laser vibrometry. Note that while accurate electric field values can be provided for the studies completed on macroscopic capacitors (c), the added voltage drop at the scanning probe tip-capacitor interface render field values incomparable; hence we report voltages in (b).

compositions with the highest value (68% for a field of 200 kV/cm) found for the $PbHf_{0.6}Ti_{0.4}O_3$ heterostructures, further confirming the observation that materials with high ε_r typically have higher tunability.[11,63,64] Next, ε_r was measured for all compositions as a function of temperature from 25 to 550 °C as noted in the Experimental Section.[65−67] With increasing titanium content, the peak in ε_r (and therefore the Curie temperature, T_C) appears to shift to higher temperatures, making the measurements more unreliable due to the higher loss tangent values at the highest temperatures probed herein. Here, data for heterostructures of composition x = 0, 0.25, 0.4, 0.45, 0.5, and 0.55 for which the loss tangent for most of the measured temperature range was <0.15 are shown (Figures 3c and S13). All the synthesized heterostructures exhibit a peak corresponding to the ferroelectric-to-paraelectric phase transition in their dielectric constant vs temperature curves. Such observations are consistent with the studies on the composition-dependent evolution of T_C in $PbZr_{1-x}Ti_xO_3$[9] as well as $PbHf_{1-x}Ti_xO_3$[44] ceramics.

Past studies on $PbHf_{1-x}Ti_xO_3$ ceramics found $PbHf_{0.5}Ti_{0.5}O_3$ as the composition corresponding to the MPB.[33,38,40,41,44,68] The presence of complex domain structures, however, can greatly influence the dielectric behavior of the mixed-phase, thin-film compositions (x = 0.4−0.55). Thus, two measurements were performed, as noted in the Experimental Section, to help better identify the location of the MPB in the films: frequency-dependent ε_r measurements with increasing DC-background bias[48,69−71] and Rayleigh studies as a function of increasing AC field.[72,73] Such studies allow for the quantification of the intrinsic/extrinsic and reversible/irreversible contributions to the dielectric response. For the first measurement, the background-DC electric field studies involved fitting the frequency-dependence (from 1 to 100 kHz) of ε_r at each value of electric field (0 to −250 kV/cm) to the equation $\varepsilon_r = \varepsilon_i - \alpha \log f$ and extracting the field-dependent intercept (ε_i) and the slope (α). As an example, we present the electric field-dependent dielectric response for one composition (x = 0.4; Figure 3d), but the datasets for the other compositions near the MPB (x = 0.4−0.55) are also provided (Figure S14). Furthermore, ε_i is plotted as a function of the applied background-DC bias for the compositions near the MPB (Figure 3e). Such plots typically show two regimes based on the contribution to the overall dielectric response. The low-field regime arises from a mixture of intrinsic (fundamental response of the polarization within a domain to applied field) and extrinsic (response due to movement of domain walls) contributions while the high-field regime provides a way to probe the intrinsic contribution (because the domain walls are pinned by the high field and are static). The intercepts, in turn, quantify the intrinsic and the extrinsic contribution to the overall dielectric response, and the slope can be considered as a form of tunability which measures how effectively the applied DC electric field can suppress the extrinsic response. For the second measurement type (i.e., Rayleigh studies), the dielectric response was recorded as a function of applied AC-excitation field at a frequency of 10 kHz with zero background-DC bias. The linear (low-field) regime of the plots was fitted to the Rayleigh law $\varepsilon_r = \varepsilon_i' + \alpha' E$, where E is the magnitude of the AC electric field and the fitting parameters ε_i' and α' are the reversible and irreversible domain-wall contributions to the overall dielectric response, respectively (inset, Figure 3e). To compare the mixed-phase compositions with the single-phase ferroelectric compositions, similar measurements were performed for $PbHf_{0.75}Ti_{0.25}O_3$ and $PbHf_{0.25}Ti_{0.75}O_3$ heterostructures (Figure S15a,b). The intercept for the linear fits in the low-field (ε_{ext}) and the high-field (ε_{int}) regimes for DC field-dependent studies and the reversible (ε_i') and irreversible (α') domain-wall contributions obtained from the linear Rayleigh fits for AC field-dependent studies have been summarized for all heterostructures (Figure 3f).

There were several observations from the DC and AC field-dependent dielectric studies worth highlighting. Overall, as expected, the mixed-phase compositions (i.e., x = 0.4−0.55) exhibit a higher ε_r as compared to the single-phase compositions (i.e., $PbHfO_3$, $PbHf_{0.75}Ti_{0.25}O_3$, $PbHf_{0.25}Ti_{0.75}O_3$, and $PbTiO_3$). As seen in the structural characterization, the presence of a dominant monoclinic phase in the mixed-phase compositions can be the reason for enhanced dielectric response owing to the ease of polarization rotation (similar to what is observed in the $PbZr_{1-x}Ti_xO_3$ system).[10,12] Delving deeper into the $PbHf_{1-x}Ti_xO_3$ compositions with the DC field-dependent studies, first, in the low-field regime, the mixed-phase compositions (x = 0.4−0.55) exhibited a considerably higher ε_{ext} (428−948) as compared to the $PbHf_{0.75}Ti_{0.25}O_3$(343) and $PbHf_{0.25}Ti_{0.75}O_3$(500) heterostructures. Within the mixed-phase compositions, ε_{ext} was the highest for the $PbHf_{0.6}Ti_{0.4}O_3$ heterostructures (948) indicating a relatively higher contribution of domain walls in the same. On the other hand, ε_{int} was the highest for the $PbHf_{0.5}Ti_{0.5}O_3$ heterostructures. This suggests that the MPB is

https://doi.org/10.1021/acs.chemmater.2c02295
Chem. Mater. 2022, 34, 9613−9623

likely close to $PbHf_{0.5}Ti_{0.5}O_3$ instead of $PbHf_{0.6}Ti_{0.4}O_3$, despite the latter showing a higher overall ε_r. Similar conclusions can be drawn from the Rayleigh studies, where the reversible (ε_i') and irreversible (α') domain-wall contributions are the highest for the $PbHf_{0.6}Ti_{0.4}O_3$ heterostructures. Such observations can be connected back to the ferroelectric measurements where the coercive field values for the $PbHf_{1-x}Ti_xO_3$ heterostructures were found to increase with increasing titanium content (likely related to the increasing tetragonal phase fraction), owing to the higher energy associated with the movement of 180° domains walls in tetragonal phases during switching.[60] Among the mixed-phase compositions, the $PbHf_{0.6}Ti_{0.4}O_3$ heterostructures should possess the lowest fraction of tetragonal phase, being closer to the rhombohedral (hafnium-rich) side of the phase diagram. Thereby, the relative ease in polarization rotation caused by the presence of non-180° domain-wall motion therein could be the reason for the higher extrinsic response in the $PbHf_{0.6}Ti_{0.4}O_3$ heterostructures (as compared to that in $PbHf_{0.5}Ti_{0.5}O_3$).

The enhanced dielectric response in the mixed-phase $PbHf_{1-x}Ti_xO_3$ compositions (x = 0.4−0.55) reinforces the idea that it is possible to realize the MPB phenomenon in a silicon-compatible system with properties similar to those observed in the archetypal $PbZr_{1-x}Ti_xO_3$. Thereby, after the structural, ferroelectric, and dielectric measurements, the electromechanical properties for the synthesized capacitor heterostructures were characterized using switching spectroscopy-based PFM as noted in the Experimental Section. Note that quantitative extraction of piezoelectric coefficients using such PFM approaches is challenging;[74−76] thus, we provide only qualitative and relative measures herein. The displacement-voltage hysteresis loops and the corresponding change in phase for 200 nm-thick $PbHf_{1-x}Ti_xO_3$ films (Figures 4a and S16) were measured, with $PbHf_{0.5}Ti_{0.5}O_3$ and $PbHf_{0.6}Ti_{0.4}O_3$ demonstrating the highest piezoelectric displacement values (Figure 4b). Though in theory, a relatively higher magnitude of enhancement in piezoelectric displacement (and coefficient, d_{33}) values would be expected for the mixed-phase compositions (x = 0.4−0.55), the same was not exactly seen in practice. This is not surprising for PFM-based measurements because some of the past studies with $PbZr_{1-x}Ti_xO_3$ films have shown similar results, where no actual composition-dependent change in the measured d_{33} values was detected for films ≤1 μm thick.[77,78] To further explore this point (and acknowledging the potential limitations of such PFM-based studies), we probed the same heterostructures using laser Doppler vibrometry as noted in the Experimental Section (Figure S17a), which allows us to directly measure the macroscopic electromechanical surface displacement of the capacitors (Figures 4c and S17b). These studies reveal that the displacement values for all heterostructures are similar in magnitude without any significant composition-dependent enhancement and are similar to that of $PbZr_{0.52}Ti_{0.48}O_3$.

It seems important to delve a bit deeper into the reasoning for such behavior. Similar to the dielectric response, the piezoelectric response too can have both intrinsic and extrinsic contributions, especially near the MPB. Unlike the dielectric response of thin films, however, observing any composition-dependent enhancement in piezoelectric response can be challenging[78,79] due to the mechanical clamping imposed by the underlying substrate suppressing the voltage-dependent piezoelectric displacement in the thin-film heterostructures. The substrate-induced clamping in such cases suppresses both the intrinsic (value expected for the material in a monodomain state) and the extrinsic (value inclusive of the movement of ferroelastic domain walls in the absence of any clamping) contributions to the piezoelectric response.[69−72] Furthermore, the thickness of the film can be a governing factor in determining the severity of substrate-induced clamping. For films with thickness ≥1 μm, restrictions on domain-wall motion were found to be severely reduced, thus leading to a more accurate estimate of the piezoelectric properties.[71,77,80,81] Due to these limitations, we turned to ab initio methods as noted in the Experimental Section to further understand the evolution of the properties near the MPB. As expected from the past studies on $PbHf_{1-x}Ti_xO_3$,[41,45] the calculated modulus values for both piezoelectric and dielectric response were found to exhibit a maximum near the mixed-phase compositions (Figure S18), further reinforcing the presence of a phase boundary therein. Thus, despite the lack of a quantitative analysis using PFM-based characterization, it is worth noting that all the heterostructures exhibited displacement values on par with that of (if not slightly better than) a reference $PbZr_{0.52}Ti_{0.48}O_3$ heterostructure (corresponding to the MPB) synthesized using identical growth parameters to the $PbHf_{1-x}Ti_xO_3$ heterostructures on a $SrRuO_3/SrTiO_3(001)$ substrate (Figure S19a−f); further pointing to the similarity between the two material systems as thin-film heterostructures and making $PbHf_{1-x}Ti_xO_3$, a promising material system for future studies concerning piezoelectric applications. As discussed earlier, despite the chemical similarity of zirconium and hafnium, zirconium is expected to be relatively more reactive with silicon than hafnium. Thus, having demonstrated the utility of the $PbHf_{1-x}Ti_xO_3$ system as a potential alternative to the $PbZr_{1-x}Ti_xO_3$ system, we also touch on potential material-design concepts based on these materials. As a single layer, $PbZr_{1-x-y}Hf_yTi_xO_3$ on silicon could be used instead of undoped $PbZr_{1-x}Ti_xO_3$ facilitating the scavenging of interfacial SiO_2 by reaction with zirconium while retaining the polar functionalities in the heterostructure with the presence of unreacted hafnium in $PbHf_{1-x}Ti_xO_3$.[11] Another example can be compositionally graded[12−14] $PbZr_{1-x-y}Hf_yTi_xO_3$ heterostructures for integration on silicon exhibiting piezoelectric loops with large voltage offsets which can exhibit a large piezoelectric response with a low dielectric constant near zero bias for MEMS applications.

CONCLUSIONS

The $PbZr_{1-x}Ti_xO_3$ system has been studied extensively because of its exceptional dielectric, piezoelectric, and ferroelectric properties. An isotypic material system which is relatively unexplored is the $PbHf_{1-x}Ti_xO_3$ system, which offers an added benefit that it can be (relatively) more compatible with integration on silicon wafers and existing CMOS fabrication processes. Here, we synthesized 50−200 nm-thick $PbHf_{1-x}Ti_xO_3$ (x = 0, 0.25, 0.4, 0.45, 0.5, 0.55, 0.75, and 1) thin-film heterostructures on $SrRuO_3/SrTiO_3(001)$ substrates. In turn, the structural, ferroelectric, dielectric, and electromechanical properties of the $PbHf_{1-x}Ti_xO_3$ thin films across the phase diagram were explored. Similar to the $PbZr_{1-x}Ti_xO_3$ system, a composition-driven structural phase transition from rhombohedral to tetragonal phases was observed with a mixed-phase [rhombohedral ($R3c$) + monoclinic (Cm) + tetragonal ($P4mm$)] structure in the composition range x = 0.4−0.55. The ferroelectric properties across the phase diagram reflected the changing crystal structure in terms of polarization and

https://doi.org/10.1021/acs.chemmater.2c02295
Chem. Mater. 2022, 34, 9613−9623

coercive-field values both of which were found to increase with increasing titanium content. Furthermore, ε_r was enhanced in the mixed-phase compositions near the MPB with the maximum value being observed for $PbHf_{0.6}Ti_{0.4}O_3$ heterostructures. Additional electric-field-dependent dielectric measurements, however, revealed that the $PbHf_{0.5}Ti_{0.5}O_3$ heterostructures are likely closer to the true MPB based on its highest intrinsic contribution to the dielectric response (similar to the observations in bulk $PbHf_{1-x}Ti_xO_3$ ceramics). The presence of ferroelectric domain walls which are relatively more mobile in $PbHf_{0.6}Ti_{0.4}O_3$ heterostructures (as compared to that in $PbHf_{0.5}Ti_{0.5}O_3$) is expected to be the primary source of an enhanced extrinsic contribution leading to an enhanced overall dielectric response. Furthermore, displacement−voltage hysteresis loops and surface displacement−electric field loops were obtained using switching spectroscopy in PFM and laser vibrometry, respectively, for all the synthesized heterostructures. While the substrate-induced quenching of domain wall motion in thin films limited the extrinsic contribution to the piezoelectric response for the mixed-phase compositions, the measured displacement values were found to be at par with that of a reference $PbZr_{0.52}Ti_{0.48}O_3$ composition, further confirming the similarity between $PbHf_{1-x}Ti_xO_3$ and $PbZr_{1-x}Ti_xO_3$ systems in terms of functionalities.

■ ASSOCIATED CONTENT

Supporting Information

The Supporting Information is available free of charge at https://pubs.acs.org/doi/10.1021/acs.chemmater.2c02295.

Reactivity of $PbHfO_3$ and $PbZrO_3$ with SiO_2; X-ray diffraction studies − lattice parameters for $PbHfO_3$; X-ray diffraction studies − lattice parameters for $PbTiO_3$; crystal structure of $PbHf_{0.75}Ti_{0.25}O_3$ and $PbHf_{0.25}Ti_{0.75}O_3$; crystal structure of $PbHf_{1-x}Ti_xO_3$ for x = 0.4, 0.45, 0.5, and 0.55; X-ray diffraction studies − lattice parameters for $PbHf_{1-x}Ti_xO_3$ ($0.25 < x < 0.75$); epitaxy of (00l)-oriented $PbHf_{1-x}Ti_xO_3$ (x = 0.25, 0.4, 0.45, 0.5, 0.55, and 0.25) films; temperature-dependent dielectric constant measurements; DC electric field-dependent dielectric constant measurements; DC/AC electric field-dependent dielectric constant measurements; PFM electromechanical studies; laser vibrometer-based electromechanical surface displacement measurements; first-principles density functional perturbation theory calculations; and characterization of reference $PbZr_{0.52}Ti_{0.48}O_3$ thin-film heterostructures (PDF)

■ AUTHOR INFORMATION

Corresponding Author

Lane W. Martin − *Department of Materials Science and Engineering, University of California, Berkeley, Berkeley, California 94720, United States; Materials Sciences Division, Lawrence Berkeley National Laboratory, Berkeley, California 94720, United States*; Email: lwmartin@berkeley.edu

Authors

Megha Acharya − *Department of Materials Science and Engineering, University of California, Berkeley, Berkeley, California 94720, United States; Materials Sciences Division, Lawrence Berkeley National Laboratory, Berkeley, California 94720, United States;* orcid.org/0000-0001-9618-1771

Handong Ling − *Department of Materials Science and Engineering, University of California, Berkeley, Berkeley, California 94720, United States; Materials Sciences Division, Lawrence Berkeley National Laboratory, Berkeley, California 94720, United States;* orcid.org/0000-0002-7776-9913

Djamila Lou − *Department of Materials Science and Engineering, University of California, Berkeley, Berkeley, California 94720, United States;* orcid.org/0000-0001-8025-2360

Maya Ramesh − *Department of Materials Science and Engineering, University of California, Berkeley, Berkeley, California 94720, United States*

Brendan Hanrahan − *DEVCOM U.S. Army Research Laboratory, Adelphi, Maryland 20783, United States*

Gabriel Velarde − *Department of Materials Science and Engineering, University of California, Berkeley, Berkeley, California 94720, United States;* orcid.org/0000-0002-7389-2017

Mark Asta − *Department of Materials Science and Engineering, University of California, Berkeley, Berkeley, California 94720, United States; Materials Sciences Division, Lawrence Berkeley National Laboratory, Berkeley, California 94720, United States;* orcid.org/0000-0002-8968-321X

Kristin Persson − *Department of Materials Science and Engineering, University of California, Berkeley, Berkeley, California 94720, United States; Materials Sciences Division and Molecular Foundry, Lawrence Berkeley National Laboratory, Berkeley, California 94720, United States*

Complete contact information is available at: https://pubs.acs.org/10.1021/acs.chemmater.2c02295

Author Contributions

M.Ac. and L.W.M. conceived of the work. M.Ac., H.L., D.L. M.R., G.V., M.As. K.P., and L.W.M. developed and implemented the methodology and experiments. M.Ac., H.L., D.L. M.R., B.H., G.V., M.As. K.P., and L.W.M. completed the formal analyses of the data. M.Ac. and L.W.M. wrote the original draft. M.Ac., H.L., B.H., G.V., M.As., K.P., and L.W.M. reviewed and edited the final manuscript. M.As., K.P., and L.W.M. provided funding and supervision for the work.

Notes

The authors declare no competing financial interest.

■ ACKNOWLEDGMENTS

This work was primarily supported by the U.S. Department of Energy, Office of Science, Office of Basic Energy Sciences, Materials Sciences and Engineering Division under Contract No. DE-AC02-05-CH11231 (Materials Project program KC23MP) for the discovery of novel functional materials. Computational resources used at the Molecular Foundry were supported by the U.S. Department of Energy, Office of Science, Office of Basic Energy Sciences under contract no. DE-AC02-05CH11231. Additional computational resources were provided by NERSC. D.L. acknowledges the support of the Army Research Office under Grant W911NF-21-1-0118 and support from the Air Force. M.R. acknowledges support from the National Science Foundation under Grant DMR-2102895. G.V. acknowledges support from the Army Research office under Grant W911NF-21-1-0126. B.H. and L.W.M. acknowledge additional support from the Army Research Laboratory as part of the Collaborative for Hierarchical Agile

and Responsive Materials (CHARM) under cooperative agreement W911NF-19-2-0119.

REFERENCES

(1) Muralt, P. Piezoelectric Thin Films for Mems. *Integr. Ferroelectr.* **1997**, *17*, 297−307.
(2) Izyumskaya, N.; Alivov, Y.-I.; Cho, S.-J.; Morkoç, H.; Lee, H.; Kang, Y.-S. Processing, Structure, Properties, and Applications of PZT Thin Films. *Crit. Rev. Solid State Mater. Sci.* **2007**, *32*, 111−202.
(3) Smith, G. L.; Pulskamp, J. S.; Sanchez, L. M.; Potrepka, D. M.; Proie, R. M.; Ivanov, T. G.; Rudy, R. Q.; Nothwang, W. D.; Bedair, S. S.; Meyer, C. D.; Polcawich, R. G. PZT-Based Piezoelectric MEMS Technology. *J. Am. Ceram. Soc.* **2012**, *95*, 1777−1792.
(4) Scott, J. F. Applications of Modern Ferroelectrics. *Science* **2007**, *315*, 954−959.
(5) Setter, N.; Damjanovic, D.; Eng, L.; Fox, G.; Gevorgian, S.; Hong, S.; Kingon, A.; Kohlstedt, H.; Park, N. Y.; Stephenson, G. B.; Stolitchnov, I.; Taganstev, A. K.; Taylor, D. V.; Yamada, T.; Streiffer, S. Ferroelectric Thin Films: Review of Materials, Properties, and Applications. *J. Appl. Phys.* **2006**, *100*, No. 051606.
(6) Jaffe, H. Piezoelectric Ceramics. *J. Am. Ceram. Soc.* **1958**, *41*, 494−498.
(7) Haun, M. J.; Furman, E.; Jang, S. J.; Cross, L. E. Thermodynamic Theory of the Lead Zirconate-Titanate Solid Solution System Part V: Theoretical Calculations. *Ferroelectrics* **1989**, *99*, 63−86.
(8) Haun, M. J.; Zhuang, Z. Q.; Furman, E.; Jang, S. J.; Cross, L. E. Thermodynamic Theory of the Lead Zirconate-Titanate Solid Solution System, Part III: Curie Constant and Sixth-Order Polarization Interaction Dielectric Stiffness Coefficients. *Ferroelectrics* **1989**, *99*, 45−54.
(9) Guo, R.; Cross, L. E.; Park, S.-E.; Noheda, B.; Cox, D. E.; Shirane, G. Origin of the High Piezoelectric Response in PbZr1-XTixO3. *Phys. Rev. Lett.* **2000**, *84*, 5423−5426.
(10) Noheda, B.; Cox, D. E.; Shirane, G.; Park, S.-E.; Cross, L. E.; Zhong, Z. Polarization Rotation via a Monoclinic Phase in the Piezoelectric 92% PbZn1/3Nb2/3O3-8% PbTiO3. *Phys. Rev. Lett.* **2001**, *86*, 3891−3894.
(11) Damjanovic, D. A Morphotropic Phase Boundary System Based on Polarization Rotation and Polarization Extension. *Appl. Phys. Lett.* **2010**, *97*, No. 062906.
(12) Noheda, B.; Cox, D. E.; Shirane, G.; Gonzalo, J. A.; Cross, L. E.; Park, S.-E. A Monoclinic Ferroelectric Phase in the Pb(Zr1−xTix)O3 Solid Solution. *Appl. Phys. Lett.* **1999**, *74*, 2059−2061.
(13) Warren, W. L.; Tuttle, B. A.; Dimos, D.; Pike, G. E.; Al-Shareef, H. N.; Ramesh, R.; Evans, J. T. Imprint in Ferroelectric Capacitors. *Jpn. J. Appl. Phys.* **1996**, *35*, No. 1521.
(14) Grossmann, M.; Lohse, O.; Bolten, D.; Boettger, U.; Schneller, T.; Waser, R. The Interface Screening Model as Origin of Imprint in PbZrxTi1−xO3 Thin Films. I. Dopant, Illumination, and Bias Dependence. *J. Appl. Phys.* **2002**, *92*, 2680−2687.
(15) Ramesh, R.; Chan, W. K.; Wilkens, B.; Gilchrist, H.; Sands, T.; Tarascon, J. M.; Keramidas, V. G.; Fork, D. K.; Lee, J.; Safari, A. Fatigue and Retention in Ferroelectric Y-Ba-Cu-O/Pb-Zr-Ti-O/Y-Ba-Cu-O Heterostructures. *Appl. Phys. Lett.* **1992**, *61*, 1537−1539.
(16) Dawber, M.; Scott, J. F. A Model for Fatigue in Ferroelectric Perovskite Thin Films. *Appl. Phys. Lett.* **2000**, *76*, 1060−1062.
(17) Jiang, A. Q.; Scott, J. F.; Dawber, M.; Wang, C. Fatigue in Artificially Layered Pb(Zr,Ti)O3 Ferroelectric Films. *J. Appl. Phys.* **2002**, *92*, 6756−6761.
(18) Scott, J. F.; de Araujo, C. A. P. Ferroelectric Memories. *Science* **1989**, *246*, 1400−1405.
(19) Bakaul, S. R.; Serrao, C. R.; Lee, M.; Yeung, C. W.; Sarker, A.; Hsu, S.-L.; Yadav, A. K.; Dedon, L.; You, L.; Khan, A. I.; Clarkson, J. D.; Hu, C.; Ramesh, R.; Salahuddin, S. Single Crystal Functional Oxides on Silicon. *Nat. Commun.* **2016**, *7*, No. 10547.
(20) McKee, R. A.; Walker, F. J.; Chisholm, M. F. Crystalline Oxides on Silicon: The First Five Monolayers. *Phys. Rev. Lett.* **1998**, *81*, 3014−3017.
(21) Haggerty, R. P.; Sarin, P.; Apostolov, Z. D.; Driemeyer, P. E.; Kriven, W. M. Thermal Expansion of HfO2 and ZrO2. *J. Am. Ceram. Soc.* **2014**, *97*, 2213−2222.
(22) Kofstad, P.; Ruzicka, D. J. On the Defect Structure of ZrO[Sub 2] and HfO[Sub 2]. *J. Electrochem. Soc.* **1963**, *110*, 181.
(23) Zheng, W.; Bowen, K. H.; Li, J.; Dabkowska, I.; Gutowski, M. Electronic Structure Differences in ZrO_2 vs HfO_2 †. *J. Phys. Chem. A* **2005**, *109*, 11521−11525.
(24) Wang, S. Q.; Mayer, J. W. Reactions of Zr Thin Films with SiO2 Substrates. *J. Appl. Phys.* **1988**, *64*, 4711−4716.
(25) Xiao, Y.; Miara, L. J.; Wang, Y.; Ceder, G. Computational Screening of Cathode Coatings for Solid-State Batteries. *Joule* **2019**, *3*, 1252−1275.
(26) Xiao, Y.; Wang, Y.; Bo, S.-H.; Kim, J. C.; Miara, L. J.; Ceder, G. Understanding Interface Stability in Solid-State Batteries. *Nat. Rev. Mater.* **2020**, *5*, 105−126.
(27) Jain, A.; Ong, S. P.; Hautier, G.; Chen, W.; Richards, W. D.; Dacek, S.; Cholia, S.; Gunter, D.; Skinner, D.; Ceder, G.; Persson, K. A. Commentary: The Materials Project: A Materials Genome Approach to Accelerating Materials Innovation. *APL Mater.* **2013**, *1*, No. 011002.
(28) Nukala, P.; Antoja-Lleonart, J.; Wei, Y.; Yedra, L.; Dkhil, B.; Noheda, B. Direct Epitaxial Growth of Polar (1 − x)HfO2−(x)ZrO2 Ultrathin Films on Silicon. *ACS Appl. Electron. Mater.* **2019**, *1*, 2585−2593.
(29) Böscke, T. S.; Müller, J.; Bräuhaus, D.; Schröder, U.; Böttger, U. Ferroelectricity in Hafnium Oxide Thin Films. *Appl. Phys. Lett.* **2011**, *99*, 102903.
(30) Cheema, S. S.; Kwon, D.; Shanker, N.; dos Reis, R.; Hsu, S.-L.; Xiao, J.; Zhang, H.; Wagner, R.; Datar, A.; McCarter, M. R.; Serrao, C. R.; Yadav, A. K.; Karbasian, G.; Hsu, C.-H.; Tan, A. J.; Wang, L.-C.; Thakare, V.; Zhang, X.; Mehta, A.; Karapetrova, E.; Chopdekar, R. V.; Shafer, P.; Arenholz, E.; Hu, C.; Proksch, R.; Ramesh, R.; Ciston, J.; Salahuddin, S. Enhanced Ferroelectricity in Ultrathin Films Grown Directly on Silicon. *Nature* **2020**, *580*, 478−482.
(31) Baek, S. H.; Park, J.; Kim, D. M.; Aksyuk, V. A.; Das, R. R.; Bu, S. D.; Felker, D. A.; Lettieri, J.; Vaithyanathan, V.; Bharadwaja, S. S. N.; Bassiri-Gharb, N.; Chen, Y. B.; Sun, H. P.; Folkman, C. M.; Jang, H. W.; Kreft, D. J.; Streiffer, S. K.; Ramesh, R.; Pan, X. Q.; Trolier-McKinstry, S.; Schlom, D. G.; Rzchowski, M. S.; Blick, R. H.; Eom, C. B. Giant Piezoelectricity on Si for Hyperactive MEMS. *Science* **2011**, *334*, 958−961.
(32) Schroeder, U.; Mueller, S.; Mueller, J.; Yurchuk, E.; Martin, D.; Adelmann, C.; Schloesser, T.; van Bentum, R.; Mikolajick, T. Hafnium Oxide Based CMOS Compatible Ferroelectric Materials. *ECS J. Solid State Sci. Technol.* **2013**, *2*, N69−N72.
(33) Strnad, N. A.; Hanrahan, B. M.; Potrepka, D. M.; Pulskamp, J. S.; Phaneuf, R. J.; Polcawich, R. G. Growth of Thin Film Ferroelectric PZT, PHT, and Antiferroelectric PHO from Atomic Layer Deposition Precursors. *J. Am. Ceram. Soc.* **2021**, *104*, 1216−1228.
(34) Corker, D. L.; Glazer, A. M.; Kaminsky, W.; Whatmore, R. W.; Dec, J.; Roleder, K. Investigation into the Crystal Structure of the Perovskite Lead Hafnate, PbHfO3. *Acta Crystallogr., Sect. B: Struct. Sci.* **1998**, *54*, 18−28.
(35) Kuprianov, M. F.; Zaitsev, S. M.; Gagarina, E. S.; Fesenko, E. G. Structural Study of PbTiO3, PbZrO3 and PbHfO3. *Phase Transitions* **1983**, *4*, 55−63.
(36) Schorn, P. J.; Schneller, T.; Böttger, U.; Waser, R. Characterization of Chemical Solution Deposition-Derived Lead Hafnate Titanate Thin Films. *J. Am. Ceram. Soc.* **2005**, *88*, 1312−1314.
(37) Lin, Y.; Zhu, J.; Wu, Z.; Luo, W.; Li, Y. Enhanced Ferroelectric Properties of Pb(Hf0.3Ti0.7)O3 Thin Films by SrRuO3 Bottom Electrode. *Ferroelectrics* **2016**, *492*, 143−149.
(38) Bedoya, C.; Muller, C.; Baudour, J.-L.; Bouree, F.; Soubeyroux, J.-L.; Roubin, M. Ferroelectric-Paraelectric Phase Transition in PbHf0.2Ti0.8O3 Studied by Neutron Powder Diffraction. *J. Phys.: Condens. Matter* **2001**, *13*, 6453.

https://doi.org/10.1021/acs.chemmater.2c02295
Chem. Mater. 2022, 34, 9613−9623

(39) Wu, Z.; Zhu, J.; Liu, X. Improved Fatigue Property of Hafnium Substitute Lead Zirconate Titanate Deposited by Pulse Laser Deposition. *J. Mater. Sci.: Mater. Electron.* **2017**, *28*, 1819−1823.
(40) Bedoya, C.; Muller, C.; Kowalski, A.; Nigrelli, E.; Roubin, M.; Leblais, J.-Y. Investigation of the Morphotropic Region in the Sr-Doped Lead Hafnate-Titanate Solid Solution Pb0. 94Sr0.06Hf1-TixO3. *J. Mater. Sci.: Mater. Electron.* **2001**, *12*, 543−550.
(41) Fantozzi, G.; Idrissi, H.; Favotto, C.; Roubin, M. Lead Hafnate Titanate (PHT) Ceramics: Processing and Properties. *J. Eur. Ceram. Soc.* **2000**, *20*, 1671−1676.
(42) Frantti, J.; Fujioka, Y.; Eriksson, S.; Hull, S.; Kakihana, M. Neutron Powder Diffraction Study of Pb(Hf x Ti1 - x)O3 Ceramics (0. 10 ≤ x ≤ 0.50). *Inorg. Chem.* **2005**, *44*, 9267−9278.
(43) Muller, C.; Baudour, J.-L.; Bedoya, C.; Bouree, F.; Soubeyroux, J.-L.; Roubin, M. Octahedral Deformations and Cationic Displacements in the Ferroelectric PbHf0. 8Ti0.2O3: A Neutron Powder Diffraction Study from 10 to 770 K. *Acta Crystallogr., Sect. B: Struct. Sci.* **2000**, *56*, 27−38.
(44) de la Rubia, M. A.; Alonso, R. E.; de Frutos, J.; López-Garcia, A. R. Phase Transitions in PbTixHf1-XO3 Determined by Thermal Analysis and Impedance Spectroscopy. *J. Therm. Anal. Calorim.* **2009**, *98*, 793.
(45) Nishio, S.; Kurokawa, F.; Tsujiura, Y.; Hida, H.; Kanno, I. Precise Piezoelectric Characterization of Pb(Hf,Ti)O3 Thin Films Deposited by Combinatorial Sputtering. *Thin Solid Films* **2016**, *616*, 444−448.
(46) Acharya, M.; Banyas, E.; Ramesh, M.; Jiang, Y.; Fernandez, A.; Dasgupta, A.; Ling, H.; Hanrahan, B.; Persson, K.; Neaton, J. B.; Martin, L. W. Exploring the Pb1−xSrxHfO3 System and Potential for High Capacitive Energy Storage Density and Efficiency. *Adv. Mater.* **2022**, *34*, No. 2105967.
(47) Mangalam, R. V. K.; Agar, J. C.; Damodaran, A. R.; Karthik, J.; Martin, L. W. Improved Pyroelectric Figures of Merit in Compositionally Graded PbZr1−x Ti x O3 Thin Films. *ACS Appl. Mater. Interfaces* **2013**, *5*, 13235−13241.
(48) Agar, J. C.; Mangalam, R. V. K.; Damodaran, A. R.; Velarde, G.; Karthik, J.; Okatan, M. B.; Chen, Z. H.; Jesse, S.; Balke, N.; Kalinin, S. V.; Martin, L. W. Tuning Susceptibility via Misfit Strain in Relaxed Morphotropic Phase Boundary PbZr1-xTixO3 Epitaxial Thin Films. *Adv. Mater. Interfaces* **2014**, *1*, No. 1400098.
(49) Baroni, S.; Giannozzi, P.; Testa, A. Green's-Function Approach to Linear Response in Solids. *Phys. Rev. Lett.* **1987**, *58*, 1861−1864.
(50) Baroni, S.; de Gironcoli, S.; Corso, A. D.; Giannozzi, P. Phonons and Related Crystal Properties from Density-Functional Perturbation Theory. *Rev. Mod. Phys.* **2001**, *73*, 515−562.
(51) de Jong, M.; Chen, W.; Geerlings, H.; Asta, M.; Persson, K. A. A Database to Enable Discovery and Design of Piezoelectric Materials. *Sci. Data* **2015**, *2*, 150053.
(52) Gonze, X. Adiabatic Density-Functional Perturbation Theory. *Phys. Rev. A: At., Mol., Opt. Phys.* **1995**, *52*, 1096−1114.
(53) Kresse, G.; Furthmüller, J. Efficient Iterative Schemes for Ab Initio Total-Energy Calculations Using a Plane-Wave Basis Set. *Phys. Rev. B: Condens. Matter Mater. Phys.* **1996**, *54*, 11169−11186.
(54) Kresse, G.; Hafner, J. Ab Initio Molecular Dynamics for Liquid Metals. *Phys. Rev. B: Condens. Matter Mater. Phys.* **1993**, *47*, 558−561.
(55) Perdew, J. P.; Burke, K.; Ernzerhof, M. Generalized Gradient Approximation Made Simple. *Phys. Rev. Lett.* **1996**, *77*, 3865−3868.
(56) Wu, X.; Vanderbilt, D.; Hamann, D. R. Systematic Treatment of Displacements, Strains, and Electric Fields in Density-Functional Perturbation Theory. *Phys. Rev. B: Condens. Matter Mater. Phys.* **2005**, *72*, No. 035105.
(57) Frantti, J.; Fujioka, Y.; Eriksson, S.; Lantto, V.; Kakihana, M. Raman Scattering Study of the Pb(HfxTi1−x)O3 Ceramics. *J. Electroceram.* **2004**, *13*, 299−303.
(58) Ducharme, S.; Fridkin, V. M.; Bune, A. V.; Palto, S. P.; Blinov, L. M.; Petukhova, N. N.; Yudin, S. G. Intrinsic Ferroelectric Coercive Field. *Phys. Rev. Lett.* **2000**, *84*, 175−178.
(59) Fridkin, V. M.; Ducharme, S. General Features of the Intrinsic Ferroelectric Coercive Field. *Phys. Solid State* **2001**, *43*, 1320−1324.
(60) Liu, S.; Grinberg, I.; Rappe, A. M. Intrinsic Ferroelectric Switching from First Principles. *Nature* **2016**, *534*, 360−363.
(61) Tagantsev, A. K.; Sherman, V. O.; Astafiev, K. F.; Venkatesh, J.; Setter, N. Ferroelectric Materials for Microwave Tunable Applications. *J. Electroceram.* **2003**, *11*, 5−66.
(62) Gu, Z.; Pandya, S.; Samanta, A.; Liu, S.; Xiao, G.; Meyers, C. J. G.; Damodaran, A. R.; Barak, H.; Dasgupta, A.; Saremi, S.; Polemi, A.; Wu, L.; Podpirka, A. A.; Will-Cole, A.; Hawley, C. J.; Davies, P. K.; York, R. A.; Grinberg, I.; Martin, L. W.; Spanier, J. E. Resonant Domain-Wall-Enhanced Tunable Microwave Ferroelectrics. *Nature* **2018**, *560*, 622−627.
(63) Budimir, M.; Damjanovic, D.; Setter, N. Piezoelectric Response and Free-Energy Instability in the Perovskite Crystals BaTiO3, PbTiO3, and Pb(Zr,Ti)O3. *Phys. Rev. B: Condens. Matter Mater. Phys.* **2006**, *73*, No. 174106.
(64) Damjanovic, D. Contributions to the Piezoelectric Effect in Ferroelectric Single Crystals and Ceramics. *J. Am. Ceram. Soc.* **2005**, *88*, 2663−2676.
(65) Asada, T.; Koyama, Y. Ferroelectric Domain Structures around the Morphotropic Phase Boundary of the Piezoelectric Material PbZr1−xTixO3. *Phys. Rev. B: Condens. Matter Mater. Phys.* **2007**, *75*, No. 214111.
(66) Wei, X.-K.; Prokhorenko, S.; Wang, B.-X.; Liu, Z.; Xie, Y.-J.; Nahas, Y.; Jia, C.-L.; Dunin-Borkowski, R. E.; Mayer, J.; Bellaiche, L.; Ye, Z.-G. Ferroelectric Phase-Transition Frustration near a Tricritical Composition Point. *Nat. Commun.* **2021**, *12*, 5322.
(67) Bdikin, I. K.; Pérez, J. A.; Coondoo, I.; Senos, A. M. R.; Mantas, P. Q.; Kholkin, A. L. Ferroelectric Domain Structure of PbZr0.35Ti0.65O3 Single Crystals by Piezoresponse Force Microscopy. *J. Appl. Phys.* **2011**, *110*, No. 052003.
(68) Li, J.; Zhu, J.; Wu, Z.; Luo, W. Influence of Hf Content on Structure and Electric Properties of PHT Thin Films with Self-Buffered Layer by PLD. *Vacuum* **2016**, *134*, 69−72.
(69) Li, S.; Cao, W.; Cross, L. E. The Extrinsic Nature of Nonlinear Behavior Observed in Lead Zirconate Titanate Ferroelectric Ceramic. *J. Appl. Phys.* **1991**, *69*, 7219−7224.
(70) Velarde, G.; Pandya, S.; Zhang, L.; Garcia, D.; Lupi, E.; Gao, R.; Wilbur, J. D.; Dames, C.; Martin, L. W. Quantifying Intrinsic, Extrinsic, Dielectric, and Secondary Pyroelectric Responses in PbZr1−x Ti x O3 Thin Films. *ACS Appl. Mater. Interfaces* **2019**, *11*, 35146−35154.
(71) Xu, F.; Trolier-McKinstry, S.; Ren, W.; Xu, B.; Xie, Z.-L.; Hemker, K. J. Domain Wall Motion and Its Contribution to the Dielectric and Piezoelectric Properties of Lead Zirconate Titanate Films. *J. Appl. Phys.* **2001**, *89*, 1336−1348.
(72) Damjanovic, D.; Demartin, M. The Rayleigh Law in Piezoelectric Ceramics. *J. Phys. D: Appl. Phys.* **1996**, *29*, 2057.
(73) Damjanovic, D.; Demartin, M. Contribution of the Irreversible Displacement of Domain Walls to the Piezoelectric Effect in Barium Titanate and Lead Zirconate Titanate Ceramics. *J. Phys.: Condens. Matter* **1997**, *9*, 4943.
(74) Kalinin, S. V.; Rar, A.; Jesse, S. A Decade of Piezoresponse Force Microscopy: Progress, Challenges, and Opportunities. *IEEE Trans. Ultrason. Ferroelectr. Freq. Control* **2006**, *53*, 2226−2252.
(75) Jesse, S.; Baddorf, A. P.; Kalinin, S. V. Dynamic Behaviour in Piezoresponse Force Microscopy. *Nanotechnology* **2006**, *17*, 1615.
(76) Jungk, T.; Hoffmann, A.; Soergel, E. Challenges for the Determination of Piezoelectric Constants with Piezoresponse Force Microscopy. *Appl. Phys. Lett.* **2007**, *91*, 253511.
(77) Yokoyama, S.; Funakubo, H.; Morioka, H.; Saito, K.; Yamada, T.; Ishikawa, M. Composition Dependency of Epitaxial Pb(Zr,Ti)O3 Films with Different Film Thickness. *Ferroelectrics* **2009**, *389*, 10−17.
(78) Nagarajan, V.; Roytburd, A.; Stanishevsky, A.; Prasertchoung, S.; Zhao, T.; Chen, L.; Melngailis, J.; Auciello, O.; Ramesh, R. Dynamics of Ferroelastic Domains in Ferroelectric Thin Films. *Nat. Mater.* **2003**, *2*, 43−47.
(79) Lefki, K.; Dormans, G. J. M. Measurement of Piezoelectric Coefficients of Ferroelectric Thin Films. *J. Appl. Phys.* **1994**, *76*, 1764−1767.

https://doi.org/10.1021/acs.chemmater.2c02295
Chem. Mater. 2022, 34, 9613−9623

(80) Jones, J. L.; Hoffman, M.; Daniels, J. E.; Studer, A. J. Direct Measurement of the Domain Switching Contribution to the Dynamic Piezoelectric Response in Ferroelectric Ceramics. *Appl. Phys. Lett.* **2006**, *89*, No. 092901.
(81) Yokoyama, S.; Honda, Y.; Morioka, H.; Okamoto, S.; Funakubo, H.; Iijima, T.; Matsuda, H.; Saito, K.; Yamamoto, T.; Okino, H.; Sakata, O.; Kimura, S. Dependence of Electrical Properties of Epitaxial Pb(Zr,Ti)O3 Thick Films on Crystal Orientation and Zr/(Zr+Ti) Ratio. *J. Appl. Phys.* **2005**, *98*, No. 094106.

https://doi.org/10.1021/acs.chemmater.2c02295
Chem. Mater. 2022, 34, 9613−9623